Hindawi
Geofluids
Volume 2022, Article ID 4484963, 11 pages
https://doi.org/10.1155/2022/4484963

Research Article

Research on Three-Phase Saturation Distribution Based on Microfluidic Visualization Experiment: A Case Study of Ling Xin Mining Area

Xiaolong Hu,[1] Hui Huang,[1] Xidong Song,[1] Hao He,[2] Xiaolong Li,[1] Jun Gao,[1] Guanghua Zhou,[1] Shaoxue Wu,[1] Guocai Kong,[1] and Xiangming Huang[1]

[1]*Ningxia Coal Industry Company Ling Xin Coal Mine, National Energy Group, Ningxia, Lingwu 751410, China*
[2]*Appraisal Center for Environment and Engineering (ACEE), Ministry of Environmental Protection, Beijing, China*

Correspondence should be addressed to Hao He; hehao@acee.org.cn

Received 4 January 2022; Accepted 22 January 2022; Published 7 July 2022

Academic Editor: Yuhe Wang

Flow characteristics and phase distribution of concentrated brine storage in mining area have been core factors linking to the leakage risk assessment and ecological evaluation. Notably, saturation plays a crucial role in impacting the flow characteristics and distribution of brine, while the existence of oil left by mining machines and original reservoir and gas produced from coal bed gas and air has complicated the issue. In this work, we conducted the microfluidic visualization experiments to reveal the saturation distribution during brine storage in mining area. We applied machine learning model to extract saturation data from experimental images with over 95% accuracy. Eventually, we found that the existence of gas significantly impacts on the saturation distribution in micropores accounting for more than 80% contribution. We clarified that the gas production rate of median 200 μL/min impacts the least on saturation variation. Results in this research are of significance for deeper comprehension on three-phase saturation characteristics of concentrated brine storage in mining area.

1. Introduction

Saturation has been proved to be a crucial parameter impacting flow characteristics of multiphase flow, especially the three-phase porous flow [1–3]. Notably, the three-phase porous flow widely exists in oil field development, soil sewage invasion, brine storage in mining area, and so on [4, 5]. Due to the fact like this, the three-phase saturation distribution (TSD) is of great significance for a deeper understanding on the three-phase porous flow and better strategies for energy development and ecological conservation [1, 6–9]. Gas production and flooding, especially during coal mining [10–12], have a nonnegligible impact on brine storage in mining area [13–16]. In specific, the residual oil in micropores is conducive to plug the predominant pathways for a better brine storage [17, 18], while the gas flooding probably displaces the brine and oil in micropores causing brine transfer, even leakage [4, 19–22].

Accordingly, effects of gas flooding and oil residence in micropores during brine storage in mining area require clarification. Since the existence of oil left by mining machines and original reservoir and gas produced from coal bed gas and air has complicated the issue, an effective method is critical. One of the most visual and effective ways to study the mechanisms of TSD by gas flooding is to conduct the visualization flooding experiments. Notably, no matter what type of rocks the reservoir consists of, the inside gas flooding process is invisible [23–25]. Exploring and describing the inside pores and fluids via imaging techniques such as CT scanning and nuclear magnetic resonance are one of the methods to achieve the visible development of reservoir by gas flooding. Due to the detail distortion caused by the conversion of photo-electric and magneto-electric signals, overlapping ambiguity, and interference of environmental factors, however, the CT scanning and nuclear magnetic resonance failed to either effectively indicate the microdetails during TSD by gas flooding or clarify the mechanisms of TSD by gas flooding [13, 15, 26–28].

The microfluidic visualization experiment is a visible experimental method for studying multiphase porous flow in microscale pores [29]. According to the parameters from actual oil reservoir, the pores in microscale are integrated onto a transparent microfluidic chip in an area of certain square centimeters. Moreover, the visualization experiments of multiphase porous flow are conducted in the microfluidic chip, which could be classified to the application category of reservoir on a chip (ROC). The core advantages of the microfluidic visualization experiment are directly visible, highly efficient, less space occupied, and chip design flexible [30–32]. The application of microfluidic visualization experiment is of great significance on clarifying the mechanisms of TSD by gas flooding and further optimizing the TSD by gas flooding technology [33–38].

In this research, we conducted the microfluidic visualization experiments according to the reservoir properties of Ling Xin mining area to reveal the saturation distribution during brine storage. We applied machine learning model to extract saturation data from experimental images. We indicated the impact of gas existence on the saturation distribution in micropores. We clarified how the gas production rate impacts on the three-phase saturation variation. Results in this research are of significance for deeper comprehension on three-phase saturation characteristics of concentrated brine storage in mining area.

2. Methodology

Figure 1 displays the route of microfluidic visualization-based mechanism and optimization research on TSD by gas flooding. The whole research was divided into microstructure design, microfluidic chip fabrication, and injection experiment, three parts. First, the target pore structure was formed by reservoir parameters restrained random micropore generation. Based on the target pore structure, the mask pattern was determined. Microfluidic chips with mask pattern were fabricated via photolithography. Afterwards, the gas flooding experiments were established based on the microfluidic chips. Flooding pressure and velocity and experimental images were measured and recorded. TSD by gas flooding was extracted via image recognition algorithm according to experimental images. Mechanisms of TSD by gas flooding were revealed while the flooding optimization was proposed from data and experimental images eventually.

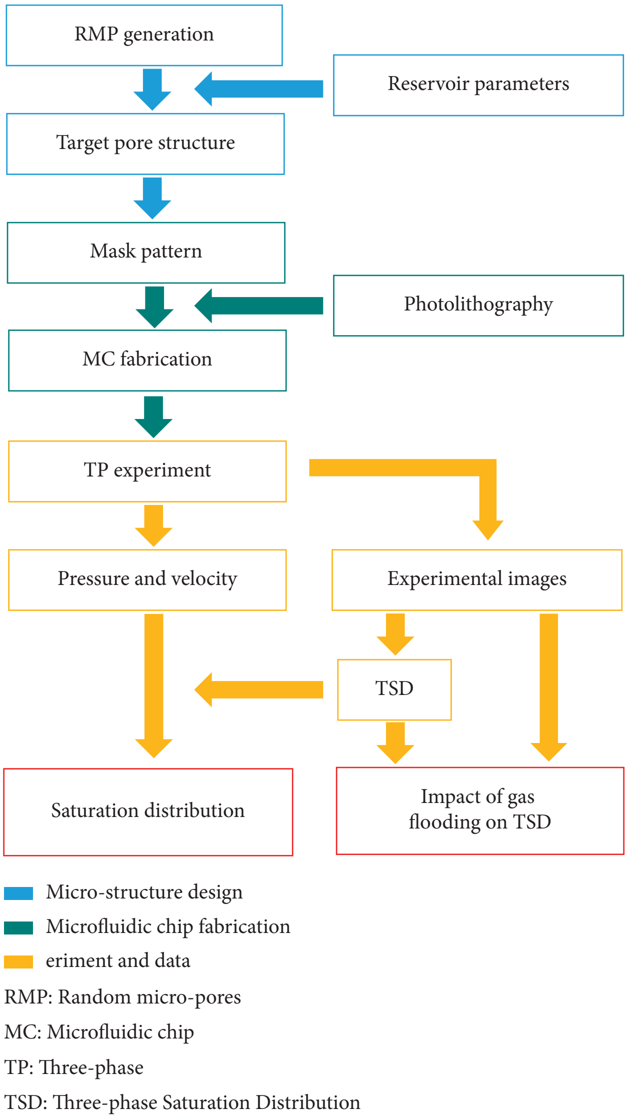

Figure 1: Route of microfluidic visualization-based mechanism and optimization research on TSD by gas flooding.

2.1. Microstructure Design. The pore structures in porous media such as the reservoir are complex and random. In general, the experimental methods only obtain statistical average features such as core porosity and permeability. While actually, to more accurately reflect the multiphase porous flow process of gas flooding in pores, the more detailed description on pore topology, connectivity, and tortuosity is required. By considering the random features of pores in oil reservoir, the QSGS (quartet structure generation set) algorithm was adopted in this research for generating the pore structures with high similarity to oil reservoir [39]. Moreover, the QSGS algorithm was improved and enhanced to satisfy the demands for pore topology, connectivity, and tortuosity in this research.

Random pore generation methods and the improved QSGS algorithm adopted in this research are presented in Figure 2. Generally, there are three main methods of random pore design and generation consisting of digital core, computer assisted drawing (CAD), and optimization algorithm, as shown in Figure 2(a). The optimization algorithm, specifically the improved QSGS algorithm, was adopted in this research. Figure 2(b) presents the pore generation process of the improved QSGS. First, certain number of generation cores were distributed in the region. Afterwards, the generation cores grew in eight directions at given probabilities and occupied the blank region constantly, forming blocks in the region. Compared with the original QSGS, the improved QSGS would judge whether the next

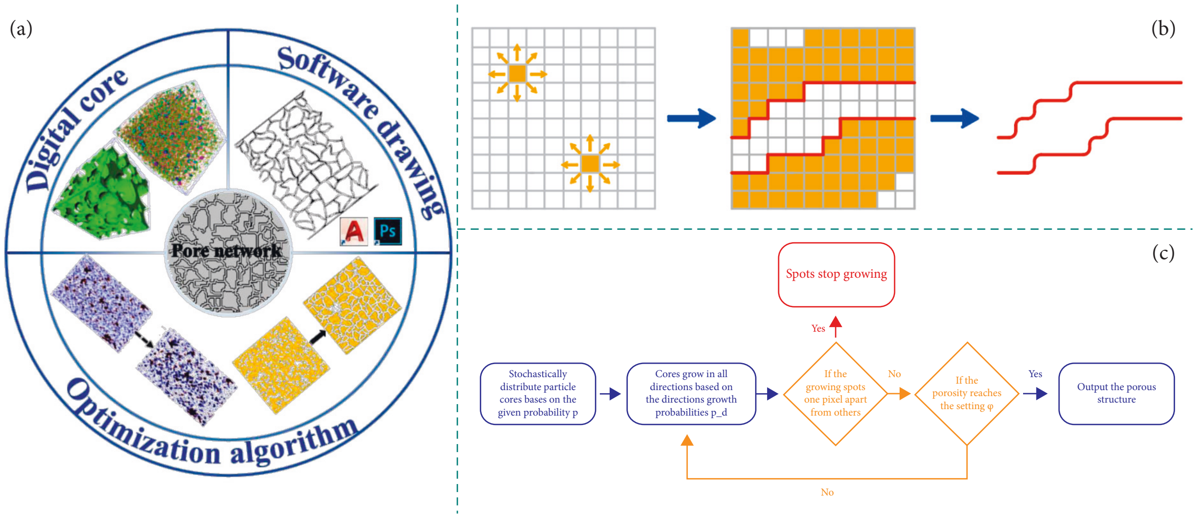

FIGURE 2: Random pore generation methods and the improved QSGS algorithm adopted in this research.

step growth resulted in the connection of two blocks or not. If so, the improved QSGS would stop the growth of blocks in the connection direction to ensure the fine connectivity of generated pores. When the porosity reached the setting value, the improved QSGS ended and output the final generated pore structure. Route of pore generation by improved QSGS could be seen in Figure 2(c) [40, 41].

2.2. Microfluidic Device Fabrication. The microfluidic chip was fabricated in laboratory at room temperature 24.3°C and relative humidity 70%. The first step was to fabricate the male mold. First, the silicon wafer was cleaned via ultrasonication at 120 W in 10 minutes. Then, the SU8-3050 negative photoresist was coat spun upon the silicon wafer. Afterwards, the photoresist coated silicon wafer was soft baked at 95°C for 10 minutes. Next, the wafer was put in vacuum chamber, covered by the designed mask and exposed in UV light at 50 mW/cm^2 for 10 seconds. The exposed wafer was postexpose baked at initially 65°C for 2 minutes and at 95°C for 8 minutes later. After this, the wafer was put in the PGMEA (propylene glycol methyl ether acetate) solution for 8-minute development. Eventually, the developed wafer was dried at 150°C for 10 minutes to evaporate the remaining SU-8 photoresist and fasten the male mold with the wafer [42].

The second step was to fabricate the microfluidic device. First was to mix the component A (dimethylvinyl siloxane) and component B (curing agent, dimethyl hydrosiloxane) of PDMS at the ratio of 9 : 1. Then, the PDMS was evacuated until small bubbles were completely discharged. Next, the PDMS was poured into a Petri dish placing the male mold. The Petri dish was put in a baker at 75°C to cure the PDMS. Afterwards, the PDMS device was cut out along the edge of male mold and holes were punched at inlets and outlets of the microchannels. The PDMS device was plasma treated together with the glass slide at 100 W for 1 minute, eventually was to bond the PDMS device with the glass slide with slight press and the microfluidic chips were completely fabricated. The chip was heated at 65°C for 30 minutes for stronger bonding [43, 44].

2.3. Injection Experiment Scheme. We conducted the microfluidic injection experiments at a laboratory at room temperature of 24.0°C with 80% relative humidity. The atmospheric pressure of the laboratory site was 99.2 kPa. Detailed properties of fluids used in experiments are shown in Table 1. All the fluid properties were obtained from or according to the Ling Xin mining area, China. The three-phase porous flow conducted in this work could be considered as an incompressible two-dimensional flow [45–49].

The schematic of microfluidic injection experiment and data record is presented in Figure 3, referring to the real flowing in the Ling Xin mining area, China. Generally, four modules working for the driving, pressure monitoring, experiment visualization, and data record were set. The equipment and materials contained two constant-speed microinjection pumps for liquid and gas injection, respectively. Medical plastic syringes, capsule pressure gauge, four-way valve, microfluidic chips, optical microscope with electron lens, computer system, waste collection tube, and experimental recording camera were used. The connection between equipment and materials is as shown in Figure 3. The microfluidic chip was initially saturated by the oil. The injection rate was set in the microinjection pump corresponding to the injection rate at the inlet of microfluidic chip [12, 50–54].

During the experiment, the fluid pump was switched on to inject the water. In real time, the pressure gauge showed the inlet pressure of the microfluidic chip, while the camera recorded the pressure data and the electronic lens on the microscope recorded the experimental images. Pressure data and experimental images were transmitted to the mobile workstation for storage. After the flow in the microfluidic chip stabilized, the fluid pump was stopped and the gas pump was turned on to inject gas into the microfluidic chip, starting the TSD by gas flooding experiment. The operation

Table 1: Properties of fluids used in microfluidic visualization experiments (24.3°C, 99.2 kPa).

Liquid	Density (kg/m^3)	Viscosity (mPa·s)	Compressibility (1/Pa)
Oil	855.297	4.160	5.268×10^{-10}
Brine	997.323	0.917	4.504×10^{-10}
Gas (air)	6.803	0.018	1.302×10^{-7}

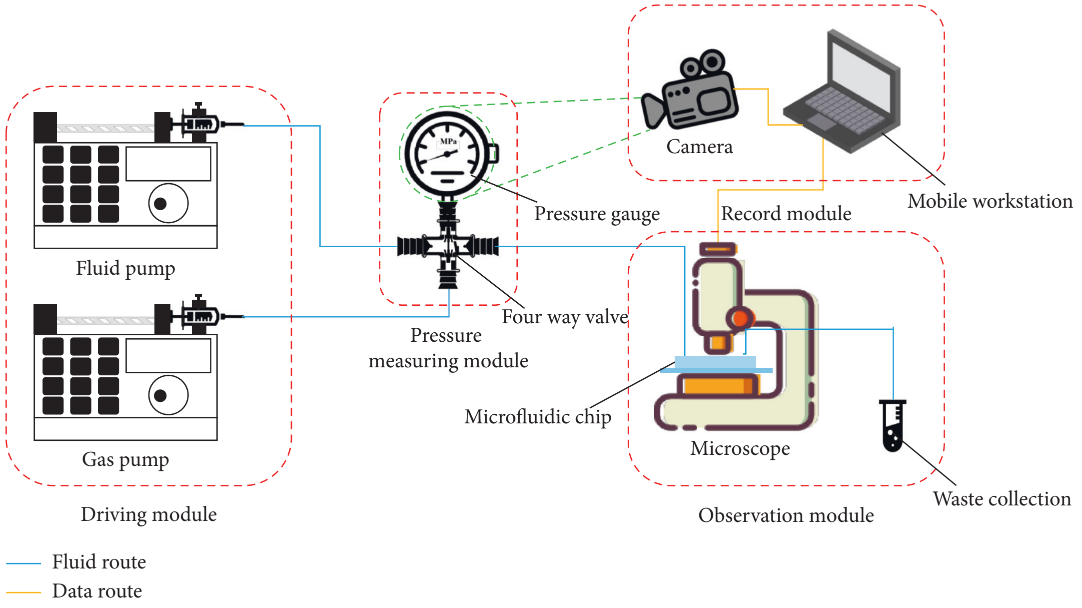

Figure 3: The schematic of microfluidic injection experiment and data record.

processes of each module were consistent with that of the water injection. After the flow in the microfluidic chip, we stabilized again, stopped the gas pump, removed the connecting pipeline between the modules, cleaned up the test table, and collected waste liquid [46, 50, 51, 55].

3. Results and Discussion

3.1. Microstructure and Microfluidic Device. In this research, the improved QSGS (quartet structure generation set) algorithm was adopted for the pore structure design and generation. The pore structure generated by original QSGS algorithm, the pore structure generated by improved QSGS algorithm, the mask pattern for microfluidic chip fabrication, and the fabricated microfluidic chip are shown in Figure 4. The size ratio on pore structure generated by improved QSGS algorithm, mask pattern, and microfluidic chip are 1 : 1 : 1 particularly.

According to Figure 4, it could be found that compared to the pore structure generated by original QSGS, the improved QSGS enhanced the connectivity of the pore structure, which was more fitting in the actual pore structures in rocks. Moreover, the improved QSGS maintained the advantages from the original version consisting of settability, high efficiency, clear physical significance, and so on. The dead zones of the pore structure were eliminated and the edges of pores were smoothed before drawing the mask pattern. Finally, the microfluidic chips with fine connectivity, topology features, and visualization were obtained.

3.2. Saturation Extracted from Experimental Images. Differed from conventional core experiments, saturation of fluids during the flooding process was extracted from experimental images based on image recognition algorithm as demonstrated in Figure 5 instead of the measurement and subtraction of fluid volume between the inlet and outlet. Besides, the gas flooding experiments conducted in this research were classified as the nonsteady state flooding method.

There were two reasons why image recognition-based saturation measurement and nonsteady state flooding method were adopted in this research. On the one hand, the microfluidic visualization experiments focused on the microscale of TSD by gas flooding. Hence, few samples were used during the complete experiments, which was hard to accurately and precisely measure the liquid volume at the microfluidic outlet. On contrast, the experimental images of fluid state in pores at every time step were zoomed in by microscope and recorded by a CCD high definition sensor. Liquid saturation and its change were easily and precisely captured and analyzed by the image recognition algorithm. On the other hand, since that the practical gas flooding in developed oil reservoirs is a nonsteady state process, the nonsteady state flooding method was applied for more appropriate research on TSD by gas flooding.

The TSD at diverse time was calculated based on the oil saturation difference captured from the image recognition algorithm. As shown in Figure 5, first a set of experimental images captured throughout the gas flooding was input into

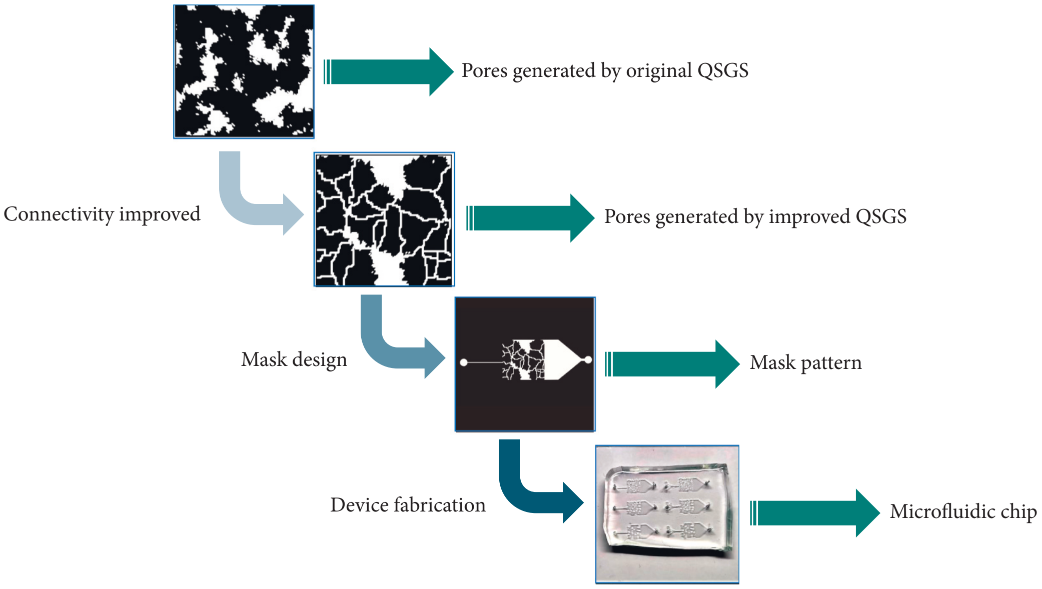

Figure 4: Generated microfluidic chip and mask based on the improved QSGS.

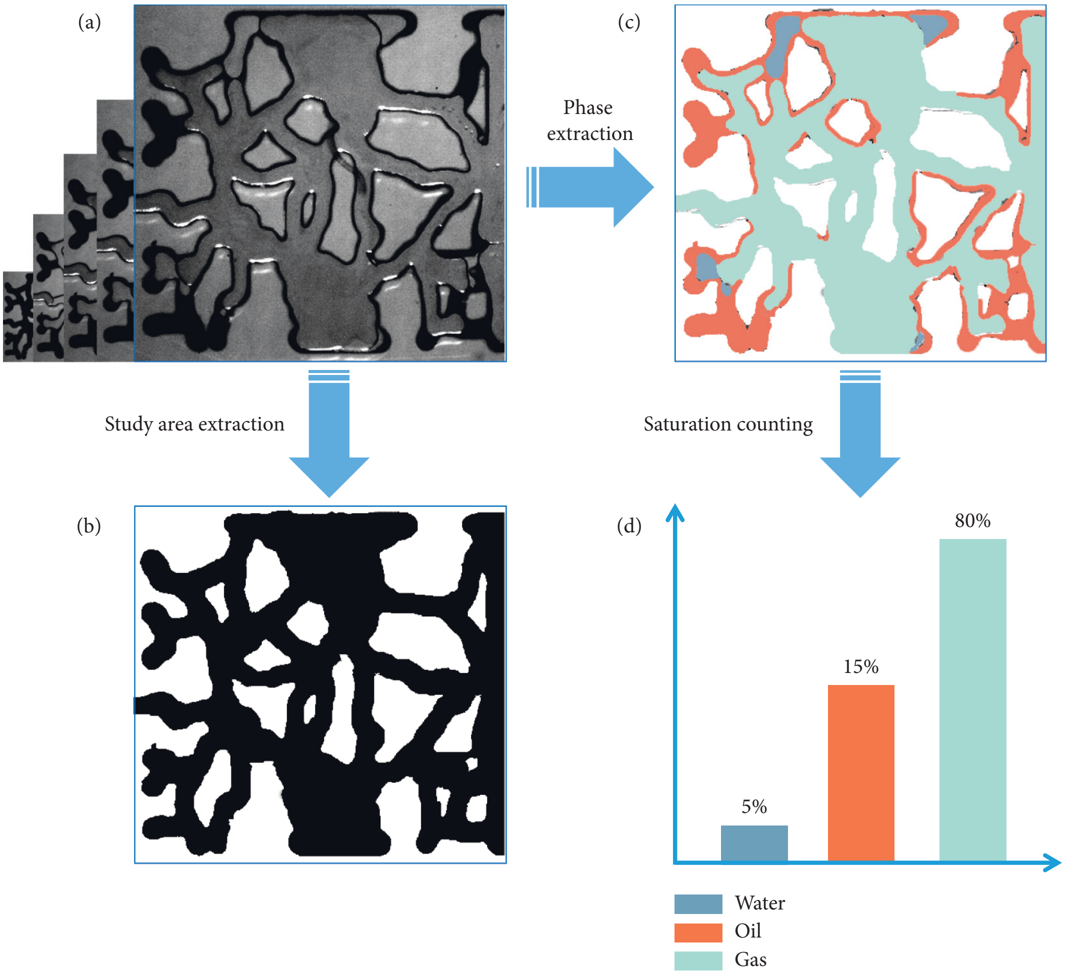

Figure 5: Saturation extracted and TSD obtained from experimental images based on image recognition algorithm.

the algorithm. The study area, the pore structure actually, and the different liquid phase were extracted by the algorithm, respectively. Then, the saturation of each type of liquid was counted. Via calculating the ratio of the saturation of each liquid at a certain moment to the initial oil saturation, the TSD at diverse time was obtained eventually.

3.3. Characteristics of Three-Phase Saturation Distribution in Mining Area. The complete process of TSD by gas flooding based on microfluidic visualization experiment is shown in Figure 6. Experiments under diverse injection rate conditions have been conducted while the specific experiment shown in Figure 6 was at the gas injection rate of 200 μL/min. The complete process included three sections. First, the pores in the microfluidic chip were saturated by oil. Next, the water was injected for oil flooding. Only the image of water flooding finished is presented in Figure 6. Last but not least, the gas was injected for oil flooding. Images of gas flooding for 6 s, 8 s, 10 s, 120 s, 1200 s, and 1500 s at which the gas flooding stopped is presented in Figure 6. The complete experiment process was designed and conducted according to the practical gas flooding in oil reservoirs. The water flooding and gas flooding were stopped when the liquid saturation and distribution in pores reached to be stable.

According to the microfluidic visualization experiment shown in Figure 6, it is worth noting that since the materials of the microfluidic chip were hydrophobic and oil wetting, oil in large pores was well displaced by water flooding while that in fine pores was residual. It could be explained that the capillary force on water was resistance which would be stronger in fine pores. Hence, water flooded through the large pores in which the capillary force resisted less.

The same thTSDy could be applied on the gas flooding. According to Figure 6, the gas invaded into the large pores and displaced the water initially before invading into the fine pores. Moreover, it could be found that the gas rapidly formed an escape path initially as shown from gas flooding for 6 s to gas flooding for 10 s in Figure 6. After the escape path was formed, the invasion of gas into pores slowed down, as shown from gas flooding for 120 s to gas flooding for 1200 s in Figure 6. Nevertheless, the TSD was achieved by gas flooding by comparing the image of water flooding finished with that of gas flooding for 1500 s in Figure 6, with a saturation contribution of 82.74%.

To further clarify the mechanism of the TSD achieved by gas flooding on microscale, Figure 7 presents the oil displacement by gas flooding via various ways in details. In Figure 7, the images of water flooding finished and that of gas flooding stopped in Figure 6 were picked for comparison to clearly present the main mechanism of the TSD by gas flooding.

According to Figure 7, two dominant mechanisms of TSD by gas flooding were presented. Mechanism A is that the gas would invade into pores that water failed to permit to enhance oil recovery. It is due to that the density and viscosity of gas are approximately 1% comparing to that of water and oil. Though the process was gradual, the gas achieved to permit into the fine pores at the similar flooding pressure of water flooding. Mechanism B is that gas would strip off the oil film attached to the pore wall to enhance oil recovery, since the injection of gas made up the pressure loss caused by stop of water flooding. It is worth noting that the mechanism A contributed more to the TSD than the mechanism B, as demonstrated in Figure 7.

3.4. Effects of Gas Production Rate on Saturation Distribution in Mining Area. In addition to clarifying the mechanisms of TSD by gas flooding, the optimization of gas flooding was studied either in this research. The core way to optimize the gas flooding is to figure out the effects of injection rate which is a crucial working condition in practical reservoir development. In this research, 100 μL/min, 200 μL/min, and 300 μL/min, three injection rates of gas flooding, were studied.

Figure 8 shows the continuous gas injection time, flooding pressure curve at diverse gas injection rate. Generally, it could be found that all curves reached a peak in certain time because of the compression of the gas at initial flooding period. Specifically, the scheme of 100 μL/min reached the peak most early while the scheme of 200 μL/min and 300 μL/min reached the peak at similar time. It is apparent that the higher the injection rate was, the higher the peak of flooding pressure could reach and the later the gas flooding achieved stability. However, it is worth noting that the relationship between injection rate and flooding pressure not strictly followed the Darcy's law, revealing a characterization of nonlinear flow. After reaching the peak, flooding pressure started to decline due to the gas decompression caused by most gas escape.

The continuous gas injection time-oil saturation curve at diverse gas injection rate is presented in Figure 9. According to Figure 9, it is surprising that there was also a nonlinear relationship between injection rate and oil saturation. More findings come out with comprehension on Figure 9 combining with Figure 8.

We observed the highest flooding pressure and shortest stabilization time, but the most remaining oil saturation at the injection flow rate of 300 μL/min. It is dominantly because the high injection rate results in serious gas escape failing to enhance oil recovery. Point A and Point B in Figure 9 respectively represent the oil saturation equivalent point of 300 μL/min with 200 μL/min and 300 μL/min with 100 μL/min, showing that the injection rate of 300 μL/min achieved the highest oil saturation initially while left behind by 200 μL/min and 100 μL/min gradually. Besides, it indicates that the scheme of 100 μL/min and 200 μL/min achieved the similar highest oil saturation where the oil saturation by gas flooding at 200 μL/min was 0.23% higher than that at 100 μL/min from Figure 9. According to Figure 8 and the mechanism A as mentioned previously, the scheme of 100 μL/min failed to offer adequate flooding pressure for gas to permit into the fine pores displacing the residual oil. Furthermore, the scheme of 200 μL/min became stable much earlier than 100 μL/min, which means it is more economical in practical reservoir development. Hence, the 200 μL/min is considered as the optimal injection rate in this research

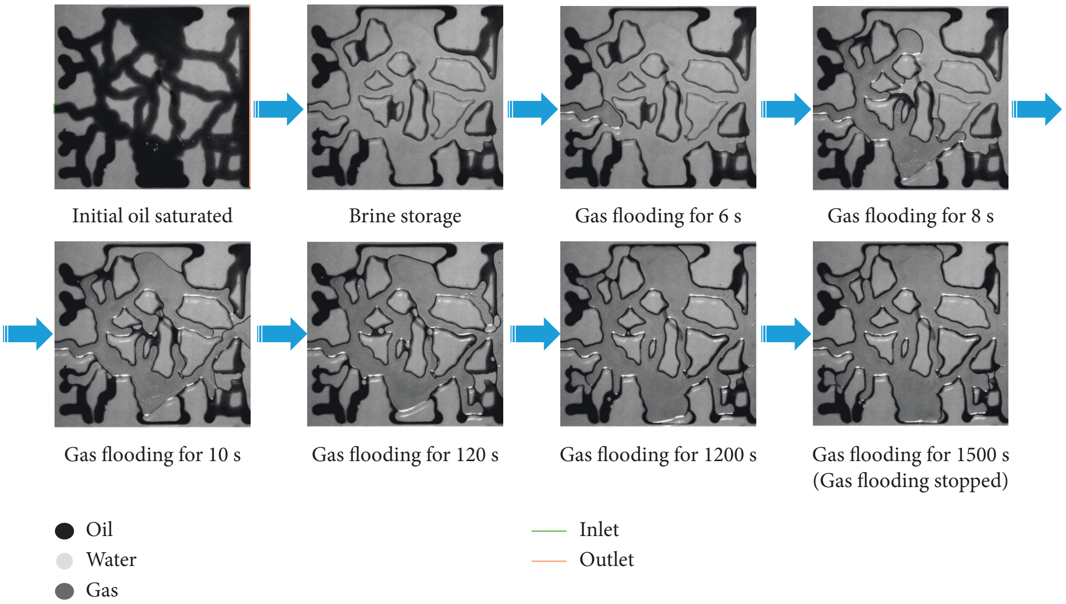

FIGURE 6: The complete process of TSD by gas flooding based on microfluidic visualization experiment.

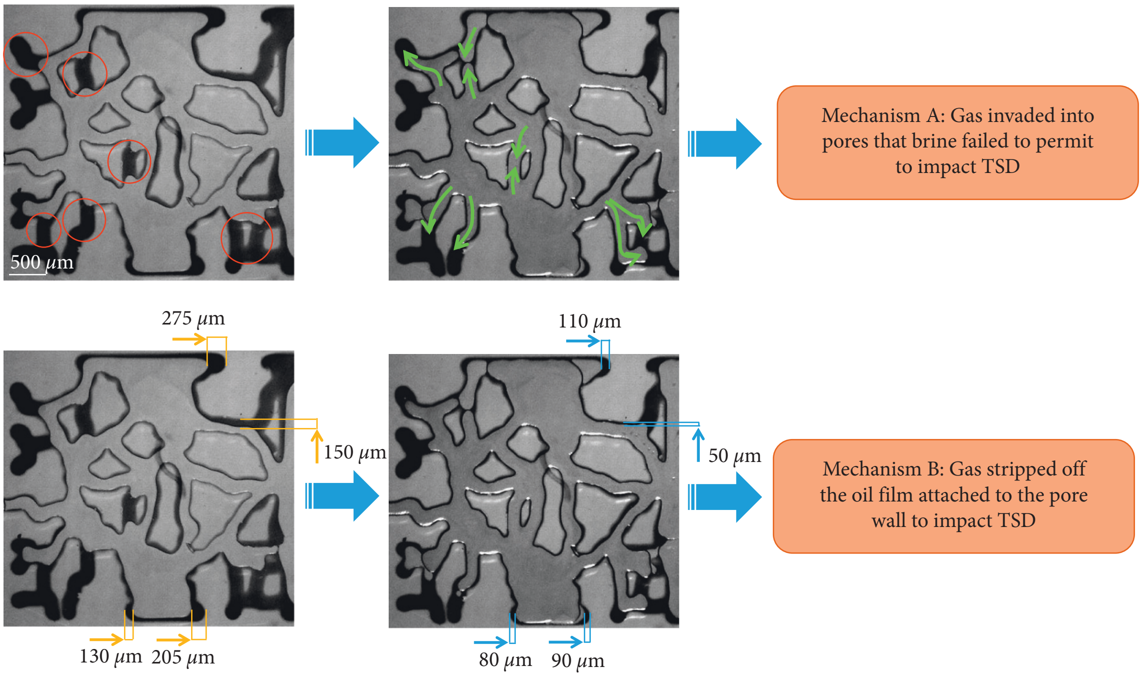

FIGURE 7: The mechanism of TSD by gas flooding based on microfluidic visualization experiment.

rather than 100 μL/min or 300 μL/min, inspiring the choice of injection rate in practical flooding engineering.

Furthermore, to figure out the effects of gas on oil during the flooding process, the relationship between TSD and gas saturation and variation of TSD and gas saturation at diverse gas injection time of various gas injection rate were considered and studied in this research, as specifically revealed by Figures 10 and 11.

According to Figure 10, especially Figure 11, it could be found that at the initial gas flooding period, especially the first 300 s, the variety of brine saturation (Δ brine saturation) fluctuated intensively. Meanwhile, the variety of oil saturation (Δ oil saturation) fluctuated along with the Δ brine saturation showing diverse features at different injection rate, however. Particularly, the Δ brine saturation at 300 μL/min reached the peak ahead of the Δ oil saturation, which means that the gas displaced the water first and then performed the oil flooding. The same could be seen on the injection rate of 100 μL/min in Figure 11 though the peak reaching moment was 100 s behind that of 300 μL/min. It is worth noting that at 200 μL/min, the raising and decreasing periods of Δ brine saturation and Δ oil saturation were

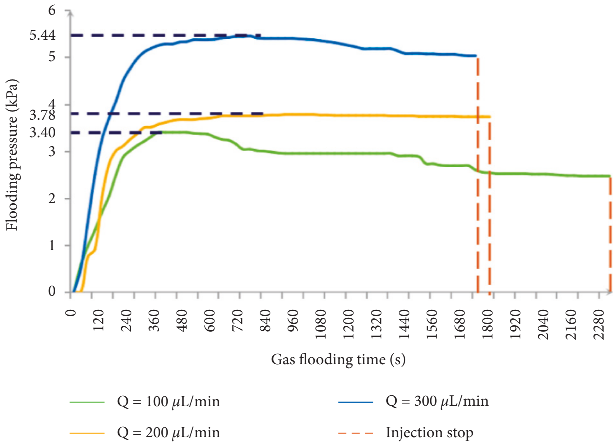

Figure 8: The continuous gas injection time-flooding pressure curve at diverse gas injection rate.

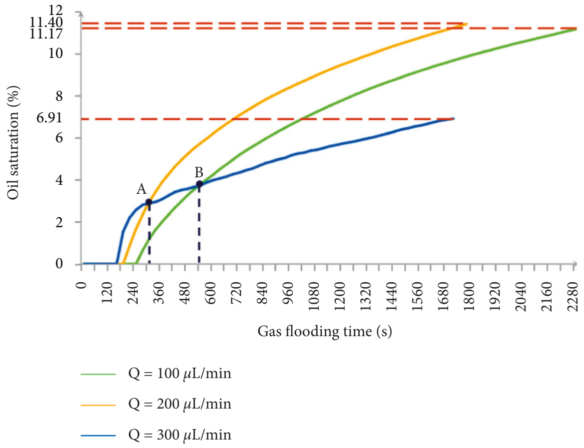

Figure 9: The continuous gas injection time-TSD curve at diverse gas injection rate.

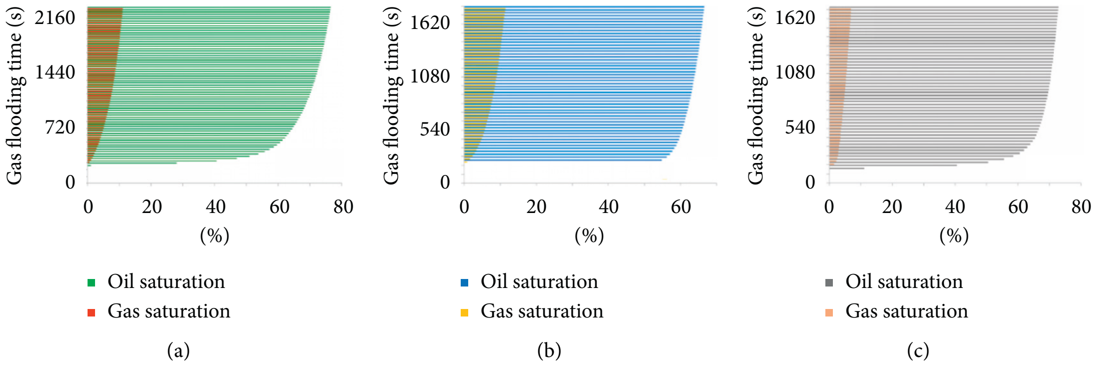

(a) (b) (c)

Figure 10: The relationship between TSD and gas saturation at diverse gas injection times. (a) $Q = 100\,\mu$L/min; (b) $Q = 200\,\mu$L/min; (c) $Q = 300\,\mu$L/min.

coincident demonstrating that the gas displaced the oil and water simultaneously, which is valuable in practical reservoir development. It also indicates that the injection rate of 200 μL/min in this research was the optimal injection rate from another point of view.

In the middle and later periods of gas flooding, especially after 500 s injection, both the Δ brine saturation and Δ oil saturation declined at a similar rate no matter what injection rate it was according to Figure 11. Hence, in the middle and later periods, water had been mostly displaced by the gas and the gas started to flood the oil directly based on both mechanism A and mechanism B. Nonetheless, the most crucial period of oil saturation by gas flooding was the initial injection, comprehensively based on Figures 10 and 11.

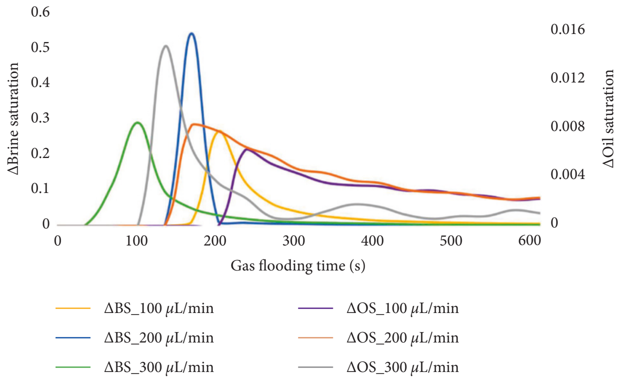

Figure 11: The variation of TSD and gas saturation of various gas injection rates at diverse gas injection times.

4. Conclusion

The flow characteristics and phase distribution of concentrated brine storage in mining area have been core factors linking to the leakage risk assessment and ecological evaluation. Notably, saturation plays a crucial role in impacting the flow characteristics and distribution of brine, while the existence of oil left by mining machines and original reservoir and gas produced from coal bed gas and air has complicated the issue.

In this work, we conducted the microfluidic visualization experiments to reveal the saturation distribution during brine storage in mining area. We applied machine learning model to extract saturation data from experimental images with over 95% accuracy. Eventually, we found that the existence of gas significantly impacts on the saturation distribution in micropores accounting for more than 80% contribution, while the oil contributed nearly 15%. We clarified that the gas production rate of median 200 μL/min from the scheme of 100 μL/min, 200 μL/min, and 300 μL/min impacts the least on saturation variation. In general, advantages including visualization and high efficiency of microfluidic technology have boosted the enhancement and optimization of three-phase saturation distribution researches in mining area. Results in this research are of significance for deeper comprehension on three-phase saturation characteristics of concentrated brine storage in mining area.

Data Availability

Data are available on request. Please contact the corresponding author for the underlying data supporting the results of the research.

Conflicts of Interest

The authors declare that there are no conflicts of interest regarding the publication of this article.

Acknowledgments

The authors are grateful for financial support from the National Energy Group Ningxia Coal Industry Company Lingxin Coal Industry Demonstration Project (Environmental Risk Research of Underground Brine Storage Reservoir in Mining Area), Open Fund of Chinese State Key Laboratory of Water Resource Protection and Utilization in Coal Mining with grant number SHJT-16-30.3.

References

[1] D. N. Rao and M. G. Girard, "Induced multiphase flow behaviour effects in gas injection TSD projects," *Journal of Canadian Petroleum Technology*, vol. 41, no. 7, pp. 53–60, 2002.

[2] X. Guo, X. G. Meng, Z. M. Du, M. Zhou, T. T. Xing, and C. W. Wang, "Studies on foam flooding for high salinity reservoirs after polymer flooding," *Oil Gas: European Magazine*, vol. 41, no. 2, pp. 103–109, 2015.

[3] Z. Pang, H. Liu, and L. Zhu, "A laboratory study of enhancing heavy oil recovery with steam flooding by adding nitrogen foams," *Journal of Petroleum Science and Engineering*, vol. 128, pp. 184–193, 2015.

[4] J. Zhang, H. Q. Song, W. Y. Zhu, and J. L. Wang, "Liquid transport through nanoscale porous media with strong wettability," *Transport in Porous Media*, vol. 140, no. 3, 2021.

[5] P. Luo, W. Luo, and S. Li, "Effectiveness of miscible and immiscible gas flooding in recovering tight oil from Bakken reservoirs in Saskatchewan, Canada," *Fuel*, vol. 208, pp. 626–636, 2017.

[6] P. Wei, W. Pu, L. Sun, and B. Wang, "Research on nitrogen foam for enhancing oil recovery in harsh reservoirs," *Journal of Petroleum Science and Engineering*, vol. 157, pp. 27–38, 2017.

[7] Y. Bai, X. Shang, Z. Wang, X. Zhao, and C. Dong, "Experimental investigation of nanolaponite stabilized nitrogen foam for enhanced oil recovery," *Energy and Fuels*, vol. 32, no. 3, pp. 3163–3175, 2018.

[8] X. Y. Guo, L. Du, P. G. Sun, J. Zhang, X. L. Shi, and H. Q. Song, "In an integrated approach to sustainable heat recovery in a sedimentary geothermal reservoir considering surface energy demands," in *Proceedings of the 10th International Conference on Applied Energy (ICAE)*, pp. 6003–6008, Hong Kong, August 2018.

[9] A. S. Hanamertani, R. M. Pilus, N. A. Manan, S. Ahmed, and M. Awang, "Ionic liquid application in surfactant foam stabilization for gas mobility control," *Energy and Fuels*, vol. 32, no. 6, pp. 6545–6556, 2018.

[10] P. Kang, J. Lao, M. Yu, H. Song, and C. Wang, "Reliable prediction on emerging energy supply for national sustainability and stability: a case study on coal bed gas supply in China based on the dual-LSTM model," *IEEE Access*, vol. 9, pp. 100694–100707, 2021.

[11] J. Lao, H. Song, C. Wang, Y. Zhou, and J. Wang, "Reducing atmospheric pollutant and greenhouse gas emissions of heavy duty trucks by substituting diesel with hydrogen in Beijing-Tianjin-Hebei-Shandong region, China," *International Journal of Hydrogen Energy*, vol. 46, no. 34, pp. 18137–18152, 2021.

[12] H. Song, H. Guo, Y. Wang et al., "A novel hybrid energy system for hydrogen production and storage in a depleted oil reservoir," *International Journal of Hydrogen Energy*, vol. 46, no. 34, pp. 18020–18031, 2021.

[13] L. Jiang, J. Sun, J. Wang et al., "The impact of ionic liquid and nanoparticles on stabilizing foam for enhanced oil recovery," *ChemistrySelect*, vol. 3, no. 44, pp. 12461–12468, 2018.

[14] S. Tang, L. Tian, J. Lu et al., "Improvement OF oil recovery through a novel low-tension foam flooding after enhanced oil

recovery processes," *Journal of Porous Media*, vol. 21, no. 3, pp. 197–208, 2018.

[15] T. Wan, W. Wang, J. Jiang, and Y. Zhang, "Pore-scale analysis of gas huff-n-puff enhanced oil recovery and waterflooding process," *Fuel*, vol. 215, pp. 561–571, 2018.

[16] A. Barati-Harooni, A. Najafi-Marghmaleki, S.-A. Hoseinpour et al., "Estimation of minimum miscibility pressure (MMP) in enhanced oil recovery (EOR) process by N2 flooding using different computational schemes," *Fuel*, vol. 235, pp. 1455–1474, 2019.

[17] H. Hematpour, S. M. Mahmood, N. H. Nasr, M. Karimi, and M. Bataee, "Experimental investigation on the mobility reduction factor of surfactant-alternating-gas foam flooding," *Kuwait J. Sci.*vol. 46, no. 4, pp. 75–82, 2019.

[18] A. Mamonov, O. A. Kvandal, S. Strand, and T. Puntervold, "Adsorption of polar organic components onto sandstone rock minerals and its effect on wettability and enhanced oil recovery potential by smart water," *Energy and Fuels*, vol. 33, no. 7, pp. 5954–5960, 2019.

[19] A. R. Namin, A. Rashidi, A. A. Gharesheikhlou, E. Ghasemy, and M. Jalilian, "Experimental application of functionalized N-doped graphene for improving enhanced oil recovery," *Colloids and Surfaces A: Physicochemical and Engineering Aspects*, p. 581, 2019.

[20] J. Wang, H. Song, V. Rasouli, and J. Killough, "An integrated approach for gas-water relative permeability determination in nanoscale porous media," *Journal of Petroleum Science and Engineering*, vol. 173, pp. 237–245, 2019.

[21] Y. Wen, M. Qu, J. Hou et al., "Experimental study on nitrogen drive and foam assisted nitrogen drive in varying-aperture fractures of carbonate reservoir," *Journal of Petroleum Science and Engineering*, vol. 180, pp. 994–1005, 2019.

[22] L. Y. Zhang, R. F. Wang, H. Q. Song et al., "Numerical investigation of techno-economic multiobjective optimization of geothermal water reservoir development: a case study of China," *Water*, vol. 11, no. 11, 2019.

[23] Q. T. Zhang, C. J. Wei, Y. H. Wang, S. Y. Du, Y. C. Zhou, and H. Q. Song, "Potential for prediction of water saturation distribution in reservoirs utilizing machine learning methods," *Energies*, vol. 12, no. 19, 2019.

[24] T. Zhang, S. Sun, and H. Song, "Flow mechanism and simulation approaches for shale gas reservoirs: a review," *Transport in Porous Media*, vol. 126, no. 3, pp. 655–681, 2019.

[25] J. H. Zhao, X. Z. Wang, H. Q. Song, Y. Du, W. J. Cui, and Y. C. Zhou, "Spatiotemporal trend analysis of PM2.5 concentration in China, 1999–2016," *Atmosphere*, vol. 10, no. 8, 2019.

[26] F. Chen, J. Gu, and X. Yao, "Laboratory evaluation and numerical simulation study on profile modification performance of gel-nitrogen-foam for low permeability formation under fracturing," *Particulate Science & Technology*, vol. 38, no. 3, pp. 299–316, 2020.

[27] X. Chu, J. He, H. Song et al., "Multimodal deep learning for heterogeneous GNSS-R data fusion and ocean wind speed retrieval," *Ieee Journal of Selected Topics in Applied Earth Observations and Remote Sensing*, vol. 13, pp. 5971–5981, 2020.

[28] S. Du, R. Wang, C. Wei et al., "The connectivity evaluation among wells in reservoir utilizing machine learning methods," *IEEE Access*, vol. 8, pp. 47209–47219, 2020.

[29] L. Y. Lang, H. B. Li, X. Wang, and N. Liu, "Experimental study and field demonstration of air-foam flooding for heavy oil TSD," *Journal of Petroleum Science and Engineering*, p. 185, 2020.

[30] Y. W. Wang, H. Q. Liu, Q. C. Zhang et al., "Pore-scale experimental study on TSD mechanisms of combining thermal and chemical flooding in heavy oil reservoirs," *Journal of Petroleum Science and Engineering*, p. 185, 2020.

[31] C. M. Xiong, B. Ding, X. F. Geng et al., "Quantitative analysis on distribution of microcosmic residual oil in reservoirs by frozen phase and nuclear magnetic resonance (NMR) technology," *Journal of Petroleum Science and Engineering*, p. 192, 2020.

[32] J. B. Yang, J. R. Hou, M. Qu, T. Liang, and Y. C. Wen, "Experimental study the flow behaviors and mechanisms of gas and foam assisted gas gas flooding in 2-D visualized fractured-vuggy model," *Journal of Petroleum Science and Engineering*, p. 194, 2020.

[33] H. F. Fan, L. Y. Zhang, R. F. Wang et al., "Investigation on geothermal water reservoir development and utilization with variable temperature regulation: a case study of China," *Applied Energy*, p. 275, 2020.

[34] H. Q. Song, S. Y. Du, R. F. Wang et al., "Potential for vertical heterogeneity prediction in reservoir basing on machine learning methods," *Geofluids*, p. 2020, 2020.

[35] H. Q. Song, J. J. Xu, J. Fang, Z. G. Cao, L. Z. Yang, and T. X. Li, "Potential for mine water disposal in coal seam goaf: investigation of storage coefficients in the Shendong mining area," *Journal of Cleaner Production*, p. 244, 2020.

[36] J. L. Wang, H. Q. Song, and Y. H. Wang, "Investigation on the micro-flow mechanism of enhanced oil recovery by low-salinity water flooding in carbonate reservoir," *Fuel*, p. 266, 2020.

[37] L. Yang, J. Xu, J. Fang, Z. Cao, T. Li, and H. Song, "Risk evaluation of groundwater leakage in coal seam goaf: a case study in the Lingxin Mining Area," *Environmental Science and Pollution Research*, vol. 27, no. 21, pp. 26066–26078, 2020.

[38] M. Yue, Q. T. Zhang, W. Y. Zhu, L. Y. Zhang, H. Q. Song, and J. H. Li, "Effects of proppant distribution in fracture networks on horizontal well performance," *Journal of Petroleum Science and Engineering*, p. 187, 2020.

[39] W. Lei, T. Liu, C. Xie, H. Yang, T. Wu, and M. Wang, "Enhanced oil recovery mechanism and recovery performance of micro-gel particle suspensions by microfluidic experiments," *Energy Science & Engineering*, vol. 8, no. 4, pp. 986–998, 2020.

[40] M. Wang, N. Pan, J. Wang, and S. Chen, "Mesoscopic simulations of phase distribution effects on the effective thermal conductivity of microgranular porous media," *Journal of Colloid and Interface Science*, vol. 311, no. 2, pp. 562–570, 2007.

[41] M. Wang, J. Wang, N. Pan, and S. Chen, "Mesoscopic predictions of the effective thermal conductivity for microscale random porous media," *Physical review. E, Statistical, nonlinear, and soft matter physics*, vol. 75, no. 3, p. 036702, 2007.

[42] L. Zhang, D. Qi, G. Zhang, C. Zhao, and H. Na, "Crosslinked tri-side-chain-type sulfonated poly(arylene ether ketones) with enhanced proton conductivity by a Friedel-Crafts acylation reaction," *RSC Advances*, vol. 4, no. 94, pp. 51916–51925, 2014.

[43] L. Zhang, L.-H. Cai, P. S. Lienemann et al., "One-step microfluidic fabrication of polyelectrolyte microcapsules in aqueous conditions for protein release," *Angewandte Chemie International Edition*, vol. 55, no. 43, pp. 13470–13474, 2016.

[44] L. Zhang, D. Qi, C. Zhao, and H. Na, "In-situ self-crosslinked sulfonated poly(arylene ether ketone) with alkyl side chain for enhanced performance," *Journal of Membrane Science*, vol. 508, pp. 15–21, 2016.

[45] D. Q. Chen, H. W. Zhao, K. Liu, Y. M. Huang, and B. F. Li, “The effect of emulsion and foam on anti-water coning during gas foam injection in bottom-water reservoirs,” *Journal of Petroleum Science and Engineering*, vol. 196, 2021.

[46] F. Rezaeiakmal and R. Parsaei, “Visualization study of polymer enhanced foam (PEF) flooding for recovery of waterflood residual oil: effect of cross flow,” *Journal of Petroleum Science and Engineering*, vol. 203, 2021.

[47] H. Q. Song, J. Zhang, D. D. Ni et al., “Investigation on in-situ water ice recovery considering energy efficiency at the lunar south pole,” *Applied Energy*, vol. 298, 2021.

[48] H. Q. Song, J. Zhang, Y. Q. Sun et al., “ThTSDetical study on thermal release of helium-3 in lunar ilmenite,” *Minerals*, vol. 11, no. 3, 2021.

[49] T. Zhang, Y. T. Li, Y. Chen et al., “Review on space energy,” *Applied Energy*, vol. 292, 2021.

[50] Y. Li, S. K. Cheng, Z. Y. Li et al., “Using system dynamics to assess the complexity of rural toilet retrofitting: case in eastern China,” *Journal of Environmental Management*, vol. 280, 2021.

[51] T. Liang and J. R. Hou, “Fluids flow behaviors of gas and foam-assisted gas floods in 2D visual fault-karst carbonate reservoir physical models,” *Journal of Petroleum Science and Engineering*, vol. 200, 2021.

[52] T. Liang, J. Hou, M. Qu et al., “Flow behaviors of nitrogen and foams in micro-visual fracture-vuggy structures,” *RSC Advances*, vol. 11, no. 45, pp. 28169–28177, 2021.

[53] M. S. Nasr, E. Esmaeilnezhad, A. Allahbakhsh, and H. J. Choi, “gas-doped graphene quantum dot nanofluids to improve oil recovery from carbonate and sandstone oil reservoirs,” *Journal of Molecular Liquids*, vol. 330, 2021.

[54] C. Y. Sie and Q. P. Nguyen, “A non-aqueous foam concept for improving hydrocarbon miscible flooding in low permeability oil formations,” *Fuel*, vol. 288, 2021.

[55] H. Z. Jiang, W. L. Kang, X. X. Li et al., “Stabilization and performance of a novel viscoelastic N-2 foam for enhanced oil recovery,” *Journal of Molecular Liquids*, vol. 337, 2021.